THE JOURNAL OF PHYSICAL CHEMISTRY C
A JOURNAL OF THE AMERICAN CHEMICAL SOCIETY

pubs.acs.org/JPCC
Article

Asymmetrical Angle-Resolved Polarized Raman Intensity Profiles Measured by Commercial Half-Wave Plates with Inevitable Retardance Error

Tao Liu,[§] Jia-Liang Xie,[§] Rui Mei, Miao-Ling Lin,* and Ping-Heng Tan*

Cite This: J. Phys. Chem. C 2024, 128, 21001−21008
Read Online

ACCESS | Metrics & More | Article Recommendations | Supporting Information

ABSTRACT: Half-wave plate (HWP) has been widely utilized in angle-resolved polarized Raman (ARPR) spectroscopy to assign Raman modes and to characterize the crystallographic orientations of anisotropic materials. Achromatic HWPs are commonly employed to control the polarization directions of the incident and Raman-scattered light over a wide spectral range. In most cases, achromatic HWPs cannot introduce a precise 180° retardance across the operating wavelength range. However, the impact of inherent retardance error from the ideal 180° retardance of the achromatic HWPs on the ARPR intensity profile remains unclear. In this study, we present a full understanding of the distinct ARPR intensity profiles of black phosphorus (BP) flakes measured with achromatic and zero-order HWPs under different polarization configurations based on the corresponding Jones matrices. A methodology to determine the unknown retardance of a HWP is proposed by fitting the ARPR intensity profiles of the A_g^2 mode in BP flakes. The results show that a HWP with as little as just over 10° in retardance error can lead to pronounced non-centrosymmetric ARPR intensity profiles; however, a HWP with retardance error less than 5° for both the incident and Raman-scattered light can be utilized in the ARPR measurements to acquire accurate and reliable ARPR intensity profile for in-plane anisotropic layered materials. Finally, we found that the configuration with a half-wave plate in the incident optical path is not desirable to unveil the quality of half-wave plates, as the ARPR intensity profile is insensitive to the retardance error. This work reveals the importance of selecting appropriate polarization configuration and proper HWP with a small retardance error to obtain reliable results of ARPR spectroscopy for anisotropic materials.

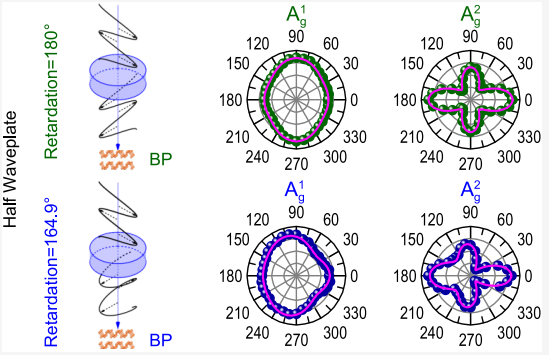

INTRODUCTION

In-plane anisotropic layered materials (ALMs) present a distinctive avenue for manipulating physical properties, due to their inherent in-plane structural anisotropy.[1−6] This anisotropy emphasizes their indispensable role in various optoelectronic devices, especially photodetectors and sensors.[7−10] Angle-resolved polarized Raman (ARPR) spectroscopy serves as a cornerstone for understanding intricacies of ALMs, which is widely employed for Raman peak assignment,[11] crystal orientation[12−15] and intrinsic Raman tensor[31] determination, and anisotropic electron−phonon interaction investigation.[15−19] Consequently, the experimental acquisition of the intrinsic ARPR intensity profile becomes imperative to ensure proper characterization and analysis of ALMs.

Half-wave plate (HWP), a commonly used birefringent optical element, introduces a relative phase retardance (α) of 180° between the light components aligned with its fast and slow axes, effectively flipping the polarization direction along the fast axis. Thus, HWPs are frequently utilized in ARPR experiments to modify the polarization states of incident light (i.e., laser) and Raman-scattered light (i.e., Raman signal). To precisely control the polarization states of light, a zero-order half-wave plate (ZHWP) is specially designed for a specific wavelength with a perfect α of 180°. Therefore, the ZHWP is generally not compatible for both incident and Raman-scattered light due to their different wavelengths. Additionally, the frequent replacement of ZHWPs is both inconvenient and inefficient to perform multi-wavelength ARPR measurements. To address this issue, an achromatic half-wave plate (AHWP) is an optimal choice for ARPR measurements, as it is supposed to keep α close to 180° over a broad wavelength range.[14,20−23] However, in this wavelength range, AHWP inevitably exhibits retardance error ($\Delta\alpha$) for both the incident and Raman-scattered light in the ARPR measurements, which refers to the discrepancy between the designed retardance and the actual one for a given

Received: October 16, 2024
Revised: November 14, 2024
Accepted: November 18, 2024
Published: November 25, 2024

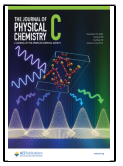

https://doi.org/10.1021/acs.jpcc.4c07013
J. Phys. Chem. C 2024, 128, 21001−21008

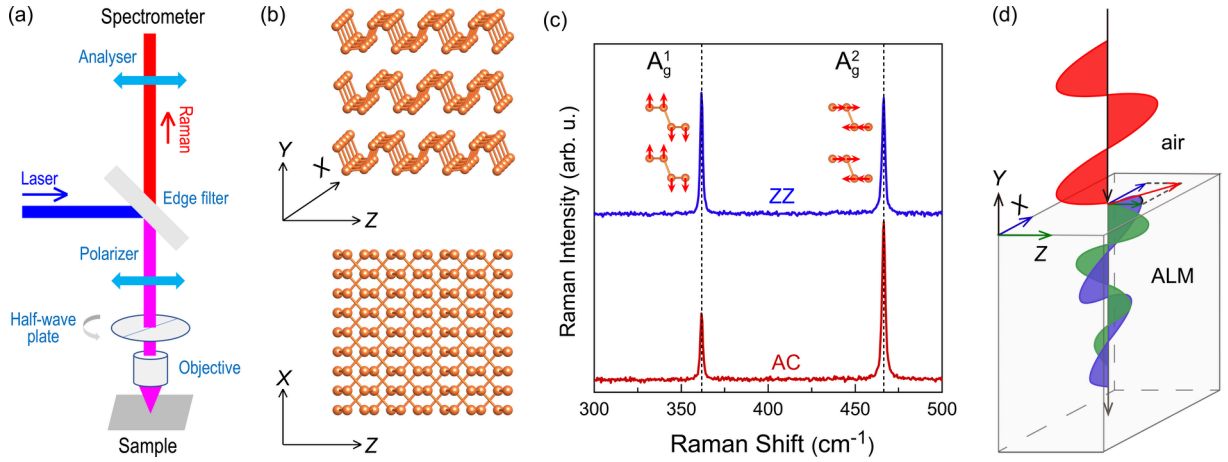

Figure 1. (a) Schematic diagram for ARPR measurements under the parallel polarization configuration, with the HWP positioned in the common optical path of incident and Raman-scattered light. (b) Crystallographic structure of BP from the side and top views. (c) Raman spectra of BP flakes with d_{BP} = 103 nm, when $\boldsymbol{e}_i$ ($\boldsymbol{e}_s$) is along the ZZ and AC axes. Inset shows the atomic displacements for the A_g^1 and A_g^2 modes. (d) Schematic illustration of the birefringence and linear dichroism effects within ALM.

wavelength. We show in this work that such $\Delta\alpha$ could have far more prominent effects than one might have thought. Therefore, one must carefully examine whether the AHWP can provide accurate and reliable ARPR results.[24−26] Indeed, AHWPs are widely used in characterizing the optical properties of anisotropic materials; however, the influence of $\Delta\alpha$ on ARPR intensity profiles has rarely been addressed. Furthermore, it is essential to clarify the impacts of $\Delta\alpha$ on the ARPR intensity profiles of ALMs under different polarization configurations[27] to select a proper polarization configuration for the corresponding ARPR measurements.

This work has two primary goals: (1) to develop an effective approach to precisely examine the retardation function $\alpha(\lambda)$ of a HWP relative to its nominal value at specific wavelength (λ); (2) to achieve accurate information on anisotropic optics and Raman tensors of ALMs for the case of a HWP with known $\Delta\alpha$ as large as being non-ignorable in the ARPR measurements. To this end, we conduct a detailed analysis of ARPR intensity profiles of black phosphorus (BP) flakes with different thickness (d_{BP}). These ARPR intensity profiles were obtained using two types of HWPs: three ZHWPs designed for three specific excitation wavelengths and two AHWPs− one with a vendor-provided $\Delta\alpha(\lambda)$ curve (AHWP#1), and another one without a $\Delta\alpha(\lambda)$ curve (AHWP#2). The measurements were performed under two commonly adopted polarization configurations. We found that when the HWP and polarizer are placed within the common optical path of the incident and Raman-scattered light (Configuration **I**), the resulting ARPR intensity profile exhibits significant sensitive dependence on $\Delta\alpha$. Typically, ARPR intensity profiles are expected to be centrosymmetric. However, we found HWPs with as little as just over 5% (~10°) in $\Delta\alpha$ can lead to pronounced non-centrosymmetric ARPR intensity profiles for the A_g^2 mode in BP flakes. This phenomenon can be adequately explained by the calculation based upon the Jones matrix of the HWP. Furthermore, the unknown $\Delta\alpha$ of HWPs can be efficiently determined by fitting the ARPR intensity profiles of the A_g^2 mode in BP flakes. We also present $\Delta\alpha$-dependent ARPR intensity profiles of bulk BP for three specific wavelengths, which can serve as a reference for rapidly evaluating the performance of HWPs. Finally, when the polarizer and HWP are placed in the incident optical path (Configuration **II**), the ARPR intensity profiles of both anisotropic BP and isotropic $MoTe_2$ flakes exhibit less dependence on $\Delta\alpha$, suggesting the application limit of Configuration **II** for ARPR measurements of ALMs.

METHODS

Sample Preparation. The BP and $MoTe_2$ flakes were exfoliated from their respective bulk materials onto polydimethylsiloxane sheets, and were subsequently transferred onto 90 nm SiO_2/Si substrates utilizing the all-dry viscoelastic stamping method.[28] The thickness of BP and $MoTe_2$ flakes was assessed using atomic force microscopy in tapping mode.

Raman Measurements. The Raman spectra were measured in backscattering geometry by using a Jobin-Yvon HR-Evolution micro-Raman system equipped with an edge filter and a charge-coupled device detector. The excitation wavelengths (λ_{ex}) were 532 nm from a solid-state laser, 633 nm from a HeNe laser, and 780 nm from a Ti:sapphire laser. Laser powers were maintained below 1.5 mW for 532 nm and 633 nm and below 10 mW for 780 nm to prevent sample heating. For ARPR measurements, a 20× microscope objective with a numerical aperture of 0.25 was employed for focusing the incident light and collecting the Raman-scattered light. A polarizer and an analyzer were aligned to ensure parallel linear polarization of the incident and Raman-scattered light. HWPs were positioned either in the common optical path (in Figure 1) or in the incident path (in Figure 6) to manipulate the polarization state of light. Two types of HWP were employed: three ZHWPs at specific wavelength of 532 nm, 633 nm, and 780 nm with a 180° retardance and AHWPs with retardances near 180° from 400 nm to 700 nm, including AHWP#1 with vendor-provided retardance curve and AHWP#2 with unknown retardance performance.

RESULTS AND DISCUSSION

ARPR Intensity Profiles of BP Flakes Measured by ZHWPs and AHWPs. The intensity of a Raman mode is determined by its Raman tensor and the corresponding polarization vectors of the incident and Raman-scattered light:[29]

$$I \propto \sum \left| \boldsymbol{e}_s^T \cdot \mathbf{R} \cdot \boldsymbol{e}_i \right|^2 \quad (1)$$

https://doi.org/10.1021/acs.jpcc.4c07013
J. Phys. Chem. C 2024, 128, 21001−21008

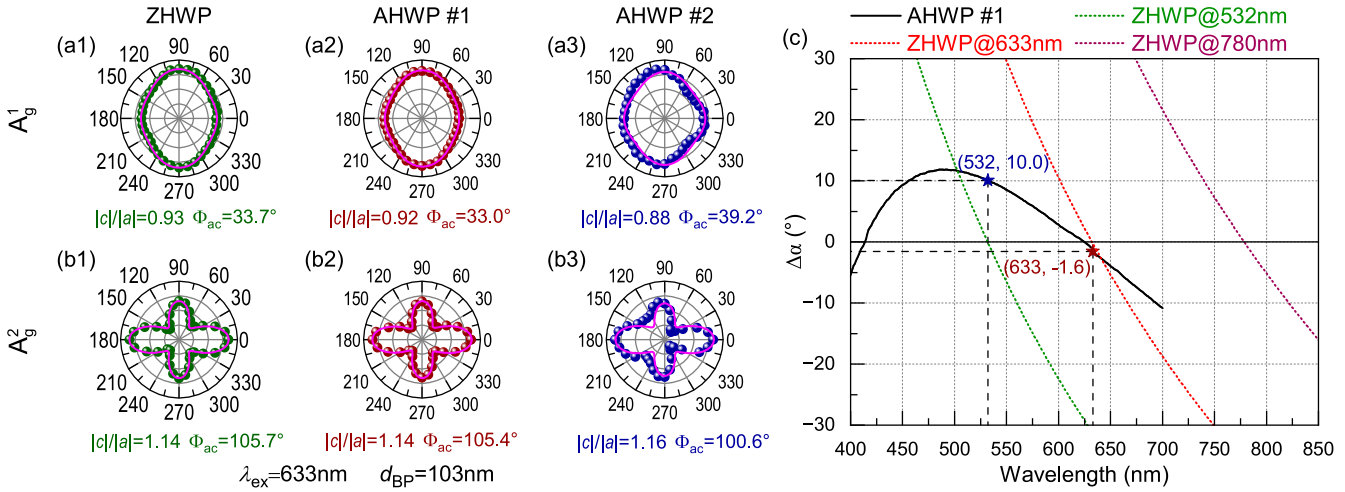

Figure 2. ARPR intensity profiles of the A_g^1 and A_g^2 modes for BP flakes with d_{BP} = 103 nm, measured under the Configuration **I** shown in Figure 1a, with λ_{ex} = 633 nm. The HWPs used for the measurements are ZHWP (a1, b1), AHWP#1 (a2, b2), and AHWP#2 (a3, b3). (c) The theoretical retardance errors $\Delta\alpha$ of AHWP#1 (solid line) and three types of ZHWPs (532 nm, 633 nm, and 780 nm, dotted lines) as a function of light wavelength. The asterisks highlight the $\Delta\alpha$ of AHWP#1 for 532 nm (dark blue) and 633 nm (magenta).

where **R** is the Raman tensor of the phonon mode and $\boldsymbol{e}_i$ and $\boldsymbol{e}_s$ are the unit polarization vectors of the incident and Raman-scattered light, respectively. Figure 1a illustrates a polarization configuration (Configuration **I**) for ARPR measurements, in which HWP and polarizer are placed in the common optical path, the analyzer is located in front of the spectrometer, and the polarization axes of the polarizer and analyzer are parallel to one another. By rotating the fast axis of the HWP in the common optical path, both $\boldsymbol{e}_i$ and $\boldsymbol{e}_s$ can be accurately controlled. BP flakes were mechanically exfoliated onto 90 nm-SiO_2/Si substrates, where the zigzag (ZZ) and armchair (AC) crystallographic directions are aligned with the X and Z axes, respectively[16] (see Figure 1b). Figure 1c displays the Raman spectra of a BP flake with d_{BP} = 103 nm excited by λ_{ex} = 633 nm for $\boldsymbol{e}_i(\boldsymbol{e}_s)\|$ZZ and $\boldsymbol{e}_i(\boldsymbol{e}_s)\|$AC. Two typical Raman modes, i.e., A_g^1 and A_g^2 modes[30] are observed at 362 cm^{-1} and 466 cm^{-1}, respectively. BP crystals exhibit evident birefringence and linear dichroism effects,[14,16−18,21,31−34] resulting in different phase velocities and penetration depths for the polarized light components aligned with the two crystallographic axes, as depicted in Figure 1d. Flake-substrate multilayer dielectrics can further modulate the light propagation within BP flakes due to the interference effects of incident and Raman-scattered light.[31,35,36] The unusual ARPR spectra in BP flakes can be explained only by considering complex Raman tensor,[17] which can be understood by the contribution from the birefringence, linear dichroism and interference effects and enables a quantitative prediction of ARPR intensity profiles of specific BP flakes deposited on dielectric substrates.[31] The Raman tensor **R** of the A_g modes in BP flakes can be described as

$$\mathbf{R}(A)_g = \begin{pmatrix} |a|e^{i\phi_a} & 0 & 0 \\ 0 & |b|e^{i\phi_b} & 0 \\ 0 & 0 & |c|e^{i\phi_c} \end{pmatrix} \quad (2)$$

The initial polarization directions of the incident and Raman-scattered light are aligned with the Z direction, denoted as $\boldsymbol{e}_i = \boldsymbol{e}_s = (0\ 0\ 1)^T$, and the Jones matrix of the HWP can be represented as follows:[37]

$$\mathbf{J}(\theta) = \begin{pmatrix} -\cos\theta & 0 & \sin\theta \\ 0 & 1 & 0 \\ \sin\theta & 0 & \cos\theta \end{pmatrix} \quad (3)$$

where θ represents twice the rotation angle $(\theta/2)$ of the HWP's fast axis relative to the Z axis. In this case, the Raman intensity of the A_g modes can be expressed by

$$I_{A_g}(\theta) \propto \left|\boldsymbol{e}_s^T \cdot \mathbf{J}(\theta)^{-1} \cdot \mathbf{R} \cdot \mathbf{J}(\theta) \cdot \boldsymbol{e}_i\right|^2 = |a|^2 \sin^4\theta + |c|^2 \cos^4\theta + 2|a||c|\sin^2\theta \cos^2\theta \cos\Phi_{ac} \quad (4)$$

where $\Phi_{ac} = \phi_c - \phi_a$.

To visualize the performances of different HWPs in the measurements of ARPR intensity profile, we conducted ARPR measurements based on the Configuration **I** at a fixed λ_{ex} of 633 nm by the corresponding ZHWP, AHWP#1 and AHWP#2, as shown in Figure 2a,b for the A_g^1 and A_g^2 modes of BP flake (d_{BP} = 103 nm). The experimental ARPR data acquired by ZHWP and AHWP#1 are in excellent agreement with the theoretical fitting curves (solid lines) based on eq 4. Furthermore, the fitting parameters obtained in both cases are highly consistent, further validating the reliability of ARPR fitting using eq 4. However, it is not the case for ARPR data acquired by AHWP#2, as illustrated in Figure 2a3,b3, e.g., the experimental results around 45° and 315° (135° and 225°) are smaller (larger) than the corresponding theoretical values, exhibiting a non-centrosymmetric ARPR intensity profiles with different fitted $|c|/|a|$ and Φ_{ac} relative to those acquired by the ZHWP and AHWP#1. In fact, it is evident that the fitted curves for AHWP#2 are significantly inconsistent with the corresponding experimental data, suggesting the existence of underlying physical origin for the measured non-centrosymmetric profiles. Interestingly, although both AHWP#1 and AHWP#2 are commercial ones designed for the measurements in the visible range, the corresponding measurements exhibit very different ARPR intensity profiles. This discrepancy may result from the nature of the retardance performances.

Due to the lack of $\Delta\alpha$ for AHWP#2, here we only demonstrated the known λ_{ex}-dependent $\Delta\alpha$ curve (i.e., $\Delta\alpha(\lambda_{ex})$) of AHWP#1 as a start to investigate the impact of

https://doi.org/10.1021/acs.jpcc.4c07013
J. Phys. Chem. C 2024, 128, 21001−21008

$\Delta\alpha$ on the ARPR intensity profile. AHWP#1 is designed for λ_{ex} in the range of 400−700 nm (solid line), and its $\Delta\alpha(\lambda_{ex})$ is presented in Figure 2c. For comparison, Figure 2c also includes the $\Delta\alpha(\lambda_{ex})$ for the three ZHWPs used in this work, designed for λ_{ex} of 532 nm, 633 nm, and 780 nm. It can be seen that AHWP#1 has reliable retardation performances over the range of 400−700 nm, demonstrating its high wavelength compatibility. In contrast, the $\Delta\alpha(\lambda_{ex})$ values of all three ZHWPs can only achieve $\Delta\alpha = 0°$ at their designed λ_{ex}. However, beyond the designed λ_{ex}, all the ZHWPs consistently display very poor compatibility, indicating that the designed λ_{ex} range of ZHWPs for applicable retardance is quite narrow. To facilitate the comparison of retardance performances between AHWP#1 and ZHWPs, the $\Delta\alpha$ of AHWP#1 at 532 nm (dark blue) and 633 nm (magenta) are marked with asterisk in Figure 2c. AHWP#1 has a $\Delta\alpha$ of −1.6° at 633 nm, which is close to that of the 633 nm ZHWP. To some extent, this explains why the ARPR intensity profiles measured with AHWP#1 and the corresponding fitted results are in agreement with those obtained by the ZHWP at λ_{ex} of 633 nm.

Figure 2c shows that the $\Delta\alpha$ of AHWP#1 has an approximate 10° deviation at 532 nm with respect to that of the corresponding ZHWP, quite different from the case at 633 nm. Such a significant $\Delta\alpha$ may have a noticeable impact on the ARPR intensity profile. Therefore, to further verify the correlation between the asymmetric ARPR intensity profiles and the $\Delta\alpha$ of the AHWPs used, we conducted ARPR measurements on the A_g^2 mode of BP flakes with different d_{BP} using both AHWP#1 and ZHWP at λ_{ex} = 532 nm, as shown in Figure 3. The ARPR intensity profiles measured with ZHWP are

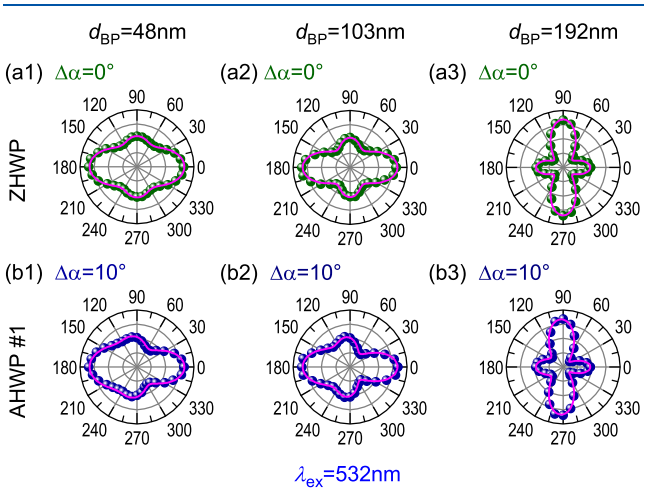

Figure 3. ARPR intensity profiles of the A_g^2 mode obtained by ZHWPs and AHWP#1 at λ_{ex} of 532 nm. (a1)−(a3) show the profiles measured by ZHWPs, while (b1)−(b3) show the profiles measured by AHWP#1.

centrosymmetric for all d_{BP} (Figure 3a). In contrast, the ARPR intensity profiles obtained with AHWP#1 lack centrosymmetry and exhibit similar distortions as in Figure 3b for all d_{BP}, in which the Raman intensity for each θ ($-90° < \theta < 90°$) is smaller than that of $\theta + 180°$. This confirms that the distortion behavior of the ARPR intensity profiles is indeed induced by the large $\Delta\alpha$ (~10°) of the AHWPs.

To precisely understand the ARPR intensity profiles measured by imperfect HWPs, real nonzero $\Delta\alpha$ should be considered for eq 3. The generalized expression for the Jones matrix of the AHWP is given below (see details in Supporting Information):[37]

$$\mathbf{J}(\theta, \Delta\alpha) = \begin{pmatrix} -\cos^2\frac{\theta}{2}e^{-i\Delta\alpha} + \sin^2\frac{\theta}{2} & 0 & (1 + e^{-i\Delta\alpha})\cos\frac{\theta}{2}\sin\frac{\theta}{2} \\ 0 & 1 & 0 \\ (1 + e^{-i\Delta\alpha})\cos\frac{\theta}{2}\sin\frac{\theta}{2} & 0 & \cos^2\frac{\theta}{2} - \sin^2\frac{\theta}{2}e^{-i\Delta\alpha} \end{pmatrix} \quad (5)$$

The incident and Raman-scattered light exhibits different wavelengths, e.g., the wavelength difference between λ_{ex} of 532 nm and the corresponding wavelength of the A_g^2 mode of BP flakes is about 13 nm, while that of the G mode in graphite can reach up to about 50 nm. Therefore, different $\Delta\alpha$ between the incident and Raman-scattered light should be considered to quantitatively interpret the measured ARPR intensity profile of the Raman mode with the frequency being fairly large for non-ignorable $\Delta\alpha$. To clarify, let $\Delta\alpha_i$ and $\Delta\alpha_s$ represent the retardance errors of the HWP at the wavelengths for the incident and Raman-scattered light, and $\mathbf{J}(\theta, \Delta\alpha_i)$ and $\mathbf{J}(\theta, \Delta\alpha_s)$ for the corresponding Jones matrices, respectively. By substituting $\mathbf{J}(\theta, \Delta\alpha_i)$ and $\mathbf{J}(\theta, \Delta\alpha_s)$ into eq 4, the Raman intensity of the A_g mode as a function of θ, $\Delta\alpha_i$, and $\Delta\alpha_s$ can be derived (similar to eq S5 in Supporting Information):

$$\begin{aligned} I_{A_g}(\theta, \Delta\alpha_i, \Delta\alpha_s) &\propto |\mathbf{e}_s^T\cdot\mathbf{J}(\theta, \Delta\alpha_s)^{-1}\cdot\mathbf{R}\cdot\mathbf{J}(\theta, \Delta\alpha_i)\cdot\mathbf{e}_i|^2 \\ &= |a|^2\cos^2\frac{\Delta\alpha_i}{2}\cos^2\frac{\Delta\alpha_s}{2}\sin^4\theta \\ &\quad + \frac{1}{16}|c|^2[4 - (1 - \cos 2\theta)(1 + \cos\Delta\alpha_i)] \\ &\quad \times [4 - (1 - \cos 2\theta)(1 + \cos\Delta\alpha_s)] \\ &\quad + 2|a||c|\cos\frac{\Delta\alpha_i}{2}\cos\frac{\Delta\alpha_s}{2}\sin^2\theta \\ &\quad \times \left(\cos\frac{\Delta\alpha_i}{2}\cos\frac{\Delta\alpha_s}{2}\cos^2\theta - \sin\frac{\Delta\alpha_i}{2}\sin\frac{\Delta\alpha_s}{2}\right) \\ &\quad \times \cos\Phi_{ac} - 2|a||c|\cos\frac{\Delta\alpha_i}{2}\cos\frac{\Delta\alpha_s}{2}\sin^2\theta\cos\theta \\ &\quad \times \sin\frac{\Delta\alpha_i + \Delta\alpha_s}{2}\sin\Phi_{ac} \end{aligned} \quad (6)$$

The three ZHWPs and AHWP#1 exhibit a small α difference less than 7.5° between the incident and Raman-scattered light of the A_g modes in BP flakes for λ_{ex} of both 532 nm, 633 nm, and 780 nm (see details in Supporting Information). Therefore, here we reasonably assume that $\Delta\alpha_s \approx \Delta\alpha_i = \Delta\alpha$, where $\Delta\alpha$ represents the retardance error of the HWP used corresponding to the incident wavelength. Based on the above approximation and eq 6, a simplified expression for the Raman intensity of the A_g modes of BP flakes can be obtained as follows,

$$\begin{aligned} I_{A_g}(\theta, \Delta\alpha) &\propto |\mathbf{e}_s^T\cdot\mathbf{J}(\theta, \Delta\alpha)^{-1}\cdot\mathbf{R}\cdot\mathbf{J}(\theta, \Delta\alpha)\cdot\mathbf{e}_i|^2 \\ &= |a|^2\cos^4\frac{\Delta\alpha}{2}\sin^4\theta + |c|^2\left(1 - \sin^2\theta\cos^2\frac{\Delta\alpha}{2}\right)^2 \\ &\quad + 2|a||c|\cos^2\frac{\Delta\alpha}{2}\sin^2\theta\left(\cos^2\frac{\Delta\alpha}{2}\cos^2\theta - \sin^2\frac{\Delta\alpha}{2}\right)\cos\Phi_{ac} \\ &\quad - \cos\theta\sin\Delta\alpha\sin\Phi_{ac} \end{aligned} \quad (7)$$

When $\Delta\alpha = 0°$, eq 7 can be simplified to eq 4, while when $\Delta\alpha \neq 0°$, $I_{A_g}(\theta, \Delta\alpha) \neq I_{A_g}(\theta + 180°, \Delta\alpha)$, except for $\theta = 0°$ or 180°, quantitatively explaining the non-centrosymmetric ARPR intensity profile measured by the AHWP#1 at λ_{ex} of 532 nm, as shown in Figure 3b.

By substituting the theoretical $\Delta\alpha$ (10°) of the AHWP#1 in Figure 2c into eq 7, we obtained the theoretical ARPR intensity

https://doi.org/10.1021/acs.jpcc.4c07013
J. Phys. Chem. C 2024, 128, 21001−21008

profiles (solid lines in Figure 3b), in good agreement with the experimental ones. Additionally, we summarized the ARPR intensity profiles of the A_g^1 mode of the corresponding BP flakes in Figure S1 of the Supporting Information, where less discrepancy was observed for the measurements by ZHWPs and AHWP#1, in contrast to the case for the A_g^2 mode. This may arise from the smaller value of Φ_{ac} for the A_g^1 mode (see details in Supporting Information).[14,17,18] Detailed analysis shows that a HWP with $\Delta\alpha$ less than 5° for both the incident and Raman-scattered light can be utilized to acquire accurate and reliable ARPR intensity profiles for ALMs in the ARPR measurements.

Determining the Unknown $\Delta\alpha$. As the ARPR intensity profiles of the A_g^2 mode of BP flakes is sensitive to $\Delta\alpha$, we can also determine the unknown $\Delta\alpha$ of specific HWP by fitting the corresponding ARPR intensity profile with eq 7. Figure 4a shows

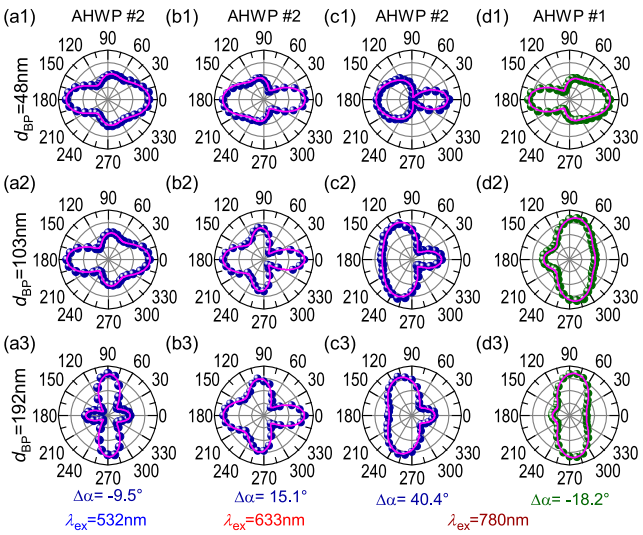

Figure 4. ARPR intensity profiles of the A_g^2 mode measured by AHWP#2 at λ_{ex} of (a) 532 nm, (b) 633 nm, and (c) 780 nm, respectively. (d) ARPR intensity profiles of the A_g^2 mode obtained with AHWP#1 for λ_{ex} = 780 nm. d_{BP} are (a1−d1) 48 nm, (a2−d2) 103 nm, and (a3−d3) 192 nm, respectively. The solid circles are experimental results. The solid lines are the fitting curves calculated with the mean fitted $\Delta\alpha$, which are labeled beneath their corresponding panels.

the ARPR intensity profiles of the A_g^2 mode for three BP flakes with varying d_{BP} for λ_{ex} = 532 nm, measured by AHWP#2. By fitting the ARPR intensity profiles with eq 7, $\Delta\alpha$ can be obtained, as shown in Table 1. All the $\Delta\alpha$ acquired from BP flakes with different d_{BP} are in close proximity to each other. The calculated ARPR intensity profiles with the average fitted $\Delta\alpha$ in

Table 1. Fitted $\Delta\alpha$ from ARPR intensity profiles of the A_g^2 mode by eq 7 in Figure 4 when λ_{ex} = 532 nm, 633 nm, and 780 nm

	$\Delta\alpha$(AHWP#2)			$\Delta\alpha$(AHWP#1)
d_{BP} (nm)	λ_{ex} = 532 nm	λ_{ex} = 633 nm	λ_{ex} = 780 nm	λ_{ex} = 780 nm
48	−10.2° ± 0.9°	15.1° ± 2.1°	43.5° ± 4.0°	−19.1° ± 1.7°
103	−10.2° ± 1.4°	16.3° ± 1.3°	41.6° ± 5.2°	−18.2° ± 1.6°
192	−8.27° ± 1.6°	14.0° ± 1.2°	36.1° ± 2.8°	−17.4° ± 0.9°
mean value	−9.5°	15.1°	40.4°	−18.2°

Table 1 based on eq 7 agree well with the experimental results. The $\Delta\alpha$ at 633 and 780 nm are determined with the similar process by fitting the ARPR intensity profiles in Figure 4b,c, as listed in Table 1. For AHWP#2, the average fitted $\Delta\alpha$ changes significantly from −9.5° at 633 nm to 40.4° at 780 nm, resulting in significant non-centrosymmetry ARPR intensity profiles. Similarly, we measured the ARPR intensity profiles by AHWP#1 at λ_{ex} of 780 nm (Figure 4d), and the fitting by eq 7 gives a mean $\Delta\alpha$ of −18.2°. The sign of $\Delta\alpha$ determines the non-centrosymmetric features of the ARPR intensity profile. For example, a positive (negative) $\Delta\alpha$ leads to smaller (larger) Raman intensity at θ ($-90° < \theta < 90°$) than that at θ + 180° in the ARPR intensity profiles of the A_g^2 mode in BP flakes, as depicted in Figure 4c,d. In addition, we utilized the average $\Delta\alpha$ fitted from the A_g^2 modes in Table 1 to predict the ARPR intensity profiles for the A_g^1 modes (Figure S2 of the Supporting Information), which are also in good agreement with the experimental ones.

To establish a standard methodology for evaluating the performance of HWPs via ARPR intensity profiles, we further illustrate the evolution of the ARPR intensity profiles of the A_g^2 mode of bulk BP ($d_{BP} > 20\ \mu m$) as $\Delta\alpha$ varies from −20° to 20° in 10° increments per step. The corresponding ARPR intensity profiles at λ_{ex} = 532 nm, 633 nm, and 780 nm are depicted in Figure 5(a-c), respectively. The intrinsic ARPR intensity profiles measured with ZHWP ($\Delta\alpha$ = 0°) exhibit centrosymmetric characteristics. With the increase in magnitude of $\Delta\alpha$, the calculated ARPR intensity profiles by eq 7 gradually deviates from centrosymmetry. The sign of $\Delta\alpha$ determines its non-centrosymmetric features, similar to the case of BP flakes (d_{BP} = 192 nm) in Figure 4. The ARPR intensity profiles at 633 and 780 nm exhibit similar evolution with $\Delta\alpha$. Thus, bulk BP ($d_{BP} > 20\ \mu m$) can be effectively utilized to evaluate the performance of a HWP.

HWP in the Incident Optical Path: Insensitive ARPR Intensity Profile to $\Delta\alpha$. We also consider another common polarization configuration[27] (Configuration **II**) for the ARPR measurements depicted in Figure 6a, where the polarizer and HWP are placed in the incident optical path. In Configuration **II**, only the polarization state of $\boldsymbol{e}_i$ is altered by rotating the HWP, while the analyzer is kept unchanged. The initial incident and Raman-scattered light polarization directions remain aligned with the Z axis, which is parallel to the AC direction of the BP flake in Figure 6b, and $\boldsymbol{e}_i = \boldsymbol{e}_s = (0\ 0\ 1)^T$. Given that only $\boldsymbol{e}_i$ is affected by the HWP, the Raman intensity of an A_g mode can be expressed as

$$I_{A_g}(\theta, \Delta\alpha) \propto |\boldsymbol{e}_s^T \cdot \mathbf{R} \cdot \mathbf{J}(\theta, \Delta\alpha) \cdot \boldsymbol{e}_i|^2 = |c|^2 \left(1 - \sin^2\theta \cos^2\frac{\Delta\alpha}{2}\right) \quad (8)$$

In this polarization configuration, the Raman tensor element ($|c|e^{i\phi_c}$) does not impact the shape of ARPR intensity profiles, and hence, the profiles for the A_g^1 and A_g^2 modes should be the same, as shown in Figure 6c,d. For λ_{ex} of 780 nm, although the difference in $\Delta\alpha$ between the ZHWP and AHWP#1 reaches up to 18.2°, as shown in Table 1, the ARPR intensity profiles measured by the ZHWP and AHWP#1 are almost the same, as depicted in Figure 6c1,c2 for the A_g^1 mode (or Figure 6d1,d2 for the A_g^2 mode). This suggests that the ARPR intensity profiles are quite insensitive to $\Delta\alpha$ in this polarization configuration. This

https://doi.org/10.1021/acs.jpcc.4c07013
J. Phys. Chem. C 2024, 128, 21001−21008

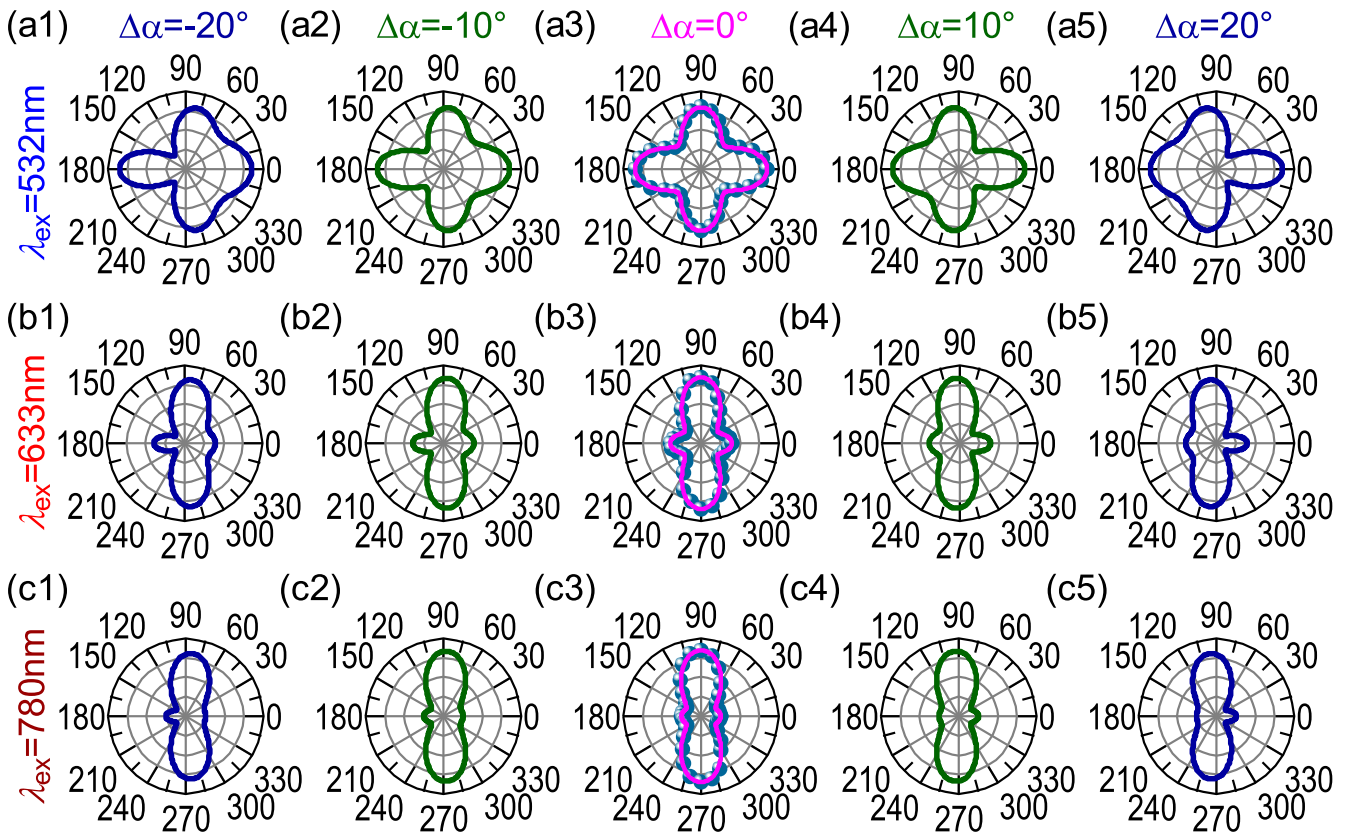

Figure 5. ARPR intensity profiles of the A_g^2 mode as a function of $\Delta\alpha$ at λ_{ex} of (a) 532 nm, (b) 633 nm, and (c) 780 nm for bulk BP with $d_{BP} > 20$ μm. Solid lines represent the fitting curves by eq 7, while experimental data measured with ZHWPs ($\Delta\alpha = 0°$) are denoted by solid circles.

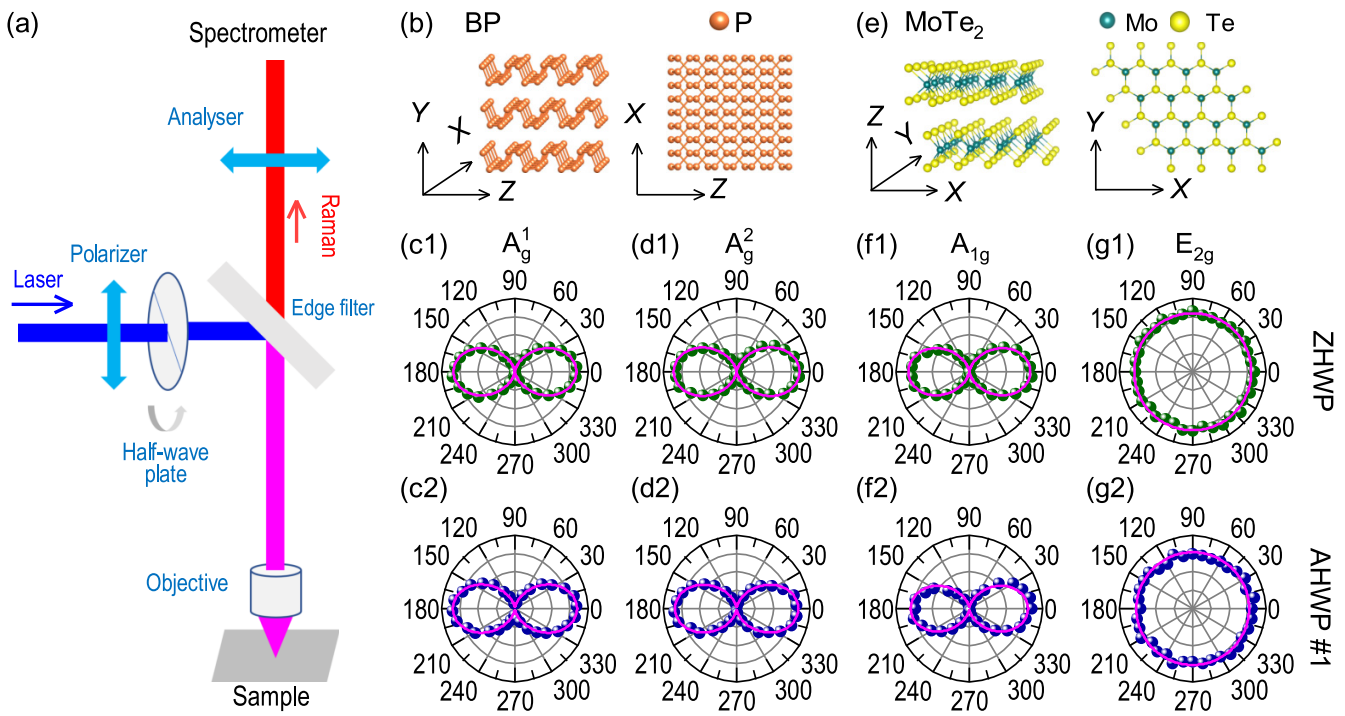

Figure 6. (a) Schematic diagram for ARPR measurements under the parallel polarization configuration, with the HWP and polarizer positioned in the incident optical path. (b) Crystallographic structure of BP from the side and top views. ARPR intensity profiles of the (c) A_g^1 and (d) A_g^2 modes of a BP flake measured by a (c1, d1) ZHWP and (c2, d2) AHWP#1. (e) Crystallographic structure of $MoTe_2$ from the side and top views. ARPR intensity profiles of the (f) A_{1g} and (g) E_{2g} modes of a $MoTe_2$ flake with thickness of 236 nm obtained by a (f1, g1) ZHWP and (f2, g2) AHWP#1. $\lambda_{ex} = 780$ nm.

https://doi.org/10.1021/acs.jpcc.4c07013
J. Phys. Chem. C 2024, 128, 21001−21008

phenomenon is understandable since only the polarization state of the incident light is changed by the HWP.

Besides the anisotropic BP, we further investigated the evolution of ARPR intensity profiles for an isotropic $MoTe_2$ flake with thickness of 236 nm to examine the above effect. Following the conventional practice, the initial polarization directions of the incident and Raman-scattered light are aligned with the X axis of $MoTe_2$ (Figure 6e), and $\boldsymbol{e}_i = \boldsymbol{e}_s = (1\ 0\ 0)^T$. The Jones matrix $\mathbf{J}'(\theta, \Delta\alpha)$ of the HWP in this coordinate system of $MoTe_2$ flakes can be written as follows:[37]

$$\mathbf{J}'(\theta, \Delta\alpha) = \begin{pmatrix} \cos^2\frac{\theta}{2} - \sin^2\frac{\theta}{2}e^{-i\Delta\alpha} & (1 + e^{-i\Delta\alpha})\cos\frac{\theta}{2}\sin\frac{\theta}{2} & 0 \\ (1 + e^{-i\Delta\alpha})\cos\frac{\theta}{2}\sin\frac{\theta}{2} & \sin^2\frac{\theta}{2} - \cos^2\frac{\theta}{2}e^{-i\Delta\alpha} & 0 \\ 0 & 0 & 1 \end{pmatrix} \tag{9}$$

The two characteristic phonons of $MoTe_2$ flakes are the A_{1g} and E_{2g} modes, whose Raman tensors are

$$\mathbf{R}\left(A_{1g}\right) = \begin{pmatrix} a' & 0 & 0 \\ 0 & a' & 0 \\ 0 & 0 & b' \end{pmatrix}, \ \mathbf{R}\left(E_{2g}\right) = \begin{pmatrix} 0 & c' & 0 \\ c' & 0 & 0 \\ 0 & 0 & 0 \end{pmatrix}, \begin{pmatrix} c' & 0 & 0 \\ 0 & -c' & 0 \\ 0 & 0 & 0 \end{pmatrix} \tag{10}$$

Thus, the ARPR intensity profiles of the A_{1g} and E_{2g} modes of $MoTe_2$ flake are expressed as follows:

$$I_{A_{1g}}(\theta, \Delta\alpha) \propto |\boldsymbol{e}_s^T \cdot \mathbf{R} \cdot \mathbf{J}'(\theta, \Delta\alpha) \cdot \boldsymbol{e}_i|^2 = |a'|^2\left(1 - \sin^2\theta \cos^2\frac{\Delta\alpha}{2}\right) \tag{11}$$

$$I_{E_{2g}}(\theta, \Delta\alpha) \propto \sum |\boldsymbol{e}_s^T \cdot \mathbf{R} \cdot \mathbf{J}'(\theta, \Delta\alpha) \cdot \boldsymbol{e}_i|^2 = |c'|^2 \tag{12}$$

Based on the above analysis, $\Delta\alpha$ has insignificant impact on the ARPR intensity profiles of the A_{1g} mode, as shown in Figure 6f, similar to the case of the A_g mode of BP flake. As for the isotropic E_{2g} mode, the Raman intensity keeps constant, independent of $\Delta\alpha$ (Figure 6g). The ARPR intensity profiles measured by AHWP#1 placed in the incident optical path resemble those of the ZHWP. Obviously, this configuration cannot discern the performance of HWPs.

When the retardance performance of a HWP is unavailable, it becomes challenging to assess the impact of $\Delta\alpha$ on the ARPR intensity profiles in Configuration **II**. In contrast, such an impact is much easier to be revealed when the HWP is placed in the common optical path (Configuration **I**, Figure 1a), as discussed above. Therefore, under the Configuration **II**, as shown in Figure 6a, the optical properties of anisotropic materials cannot be correctly probed from the corresponding ARPR intensity profiles, especially when an imperfect HWP far beyond its designed wavelength range is used for ARPR measurements.

CONCLUSIONS

We revealed the retardance error of a HWP can significantly modify the ARPR intensity profiles of BP flakes when it is placed within the common optical path of the incident and Raman-scattered light, leading to non-centrosymmetric ARPR intensity profiles. With $\Delta\alpha$ increasing, the non-centrosymmetric feature becomes more evident, which can be well reproduced by considering the Jones matrix of the HWP. Additionally, we proposed a methodology to determine the unknown retardance of a HWP. We further illustrated that the polarization configuration with a HWP and polarizer positioned in the incident optical path is not suitable for accurately quantifying the performance of the HWP by fitting ARPR intensity profiles of BP flakes. This comprehensive study significantly advances ARPR measurement techniques by the imperfect HWP for the Raman mode with the frequency as large as much for non-ignorable retardance error in the ARPR measurement.

ASSOCIATED CONTENT

Supporting Information

The Supporting Information is available free of charge at https://pubs.acs.org/doi/10.1021/acs.jpcc.4c07013.

Derivation of general form Jones matrices, general formulizm of ARPR intensity with imperfect HWP and insensitivity of A_g^1 mode (PDF)

AUTHOR INFORMATION

Corresponding Authors

Miao-Ling Lin − *State Key Laboratory of Superlattices and Microstructures, Institute of Semiconductors, Chinese Academy of Sciences, Beijing 100083, China; Center of Materials Science and Optoelectronics Engineering and CAS Center of Excellence in Topological Quantum Computation, University of Chinese Academy of Sciences, Beijing 100049, China;* orcid.org/0000-0001-5838-8237; Email: linmiaoling@semi.ac.cn

Ping-Heng Tan − *State Key Laboratory of Superlattices and Microstructures, Institute of Semiconductors, Chinese Academy of Sciences, Beijing 100083, China; Center of Materials Science and Optoelectronics Engineering and CAS Center of Excellence in Topological Quantum Computation, University of Chinese Academy of Sciences, Beijing 100049, China;* orcid.org/0000-0001-6575-1516; Email: phtan@semi.ac.cn

Authors

Tao Liu − *State Key Laboratory of Superlattices and Microstructures, Institute of Semiconductors, Chinese Academy of Sciences, Beijing 100083, China; Center of Materials Science and Optoelectronics Engineering and CAS Center of Excellence in Topological Quantum Computation, University of Chinese Academy of Sciences, Beijing 100049, China*

Jia-Liang Xie − *State Key Laboratory of Superlattices and Microstructures, Institute of Semiconductors, Chinese Academy of Sciences, Beijing 100083, China; Center of Materials Science and Optoelectronics Engineering and CAS Center of Excellence in Topological Quantum Computation, University of Chinese Academy of Sciences, Beijing 100049, China*

Rui Mei − *State Key Laboratory of Superlattices and Microstructures, Institute of Semiconductors, Chinese Academy of Sciences, Beijing 100083, China; Center of Materials Science and Optoelectronics Engineering and CAS Center of Excellence in Topological Quantum Computation, University of Chinese Academy of Sciences, Beijing 100049, China*

Complete contact information is available at: https://pubs.acs.org/10.1021/acs.jpcc.4c07013

Author Contributions

[§]These authors contributed equally to this work.

Notes

The authors declare no competing financial interest.

ACKNOWLEDGMENTS

We acknowledge the support from the National Key Research and Development Program of China (Grant No. 2023YFA1407000), the Strategic Priority Research Program of CAS (Grant No. XDB0460000), National Natural Science

Foundation of China (Grant Nos. 12322401, 12127807, and 12393832), CAS Key Research Program of Frontier Sciences (Grant No. ZDBS-LY-SLH004), Beijing Nova Program (Grant No. 20230484301), Youth Innovation Promotion Association, Chinese Academy of Sciences (No. 2023125), and CAS Project for Young Scientists in Basic Research (YSBR-026).

REFERENCES

(1) Li, L.; Yu, Y.; Ye, G. J.; Ge, Q.; Ou, X.; Wu, H.; Feng, D.; Chen, X. H.; Zhang, Y. Black Phosphorus Field-Effect Transistors. *Nat. Nanotechnol.* **2014**, *9*, 372−377.
(2) Qiao, J.; Kong, X.; Hu, Z.-X.; Yang, F.; Ji, W. High-Mobility Transport Anisotropy and Linear Dichroism in Few-Layer Black Phosphorus. *Nat. Commun.* **2014**, *5*, 4475.
(3) Xia, F.; Wang, H.; Jia, Y. Rediscovering Black Phosphorus as an Anisotropic Layered Material for Optoelectronics and Electronics. *Nat. Commun.* **2014**, *5*, 4458.
(4) Rudenko, A. N.; Brener, S.; Katsnelson, M. I. Intrinsic Charge Carrier Mobility in Single-Layer Black Phosphorus. *Phys. Rev. Lett.* **2016**, *116*, 246401.
(5) Wang, X.; Jones, A. M.; Seyler, K. L.; Tran, V.; Jia, Y.; Zhao, H.; Wang, H.; Yang, L.; Xu, X.; Xia, F. Highly Anisotropic and Robust Excitons in Monolayer Black Phosphorus. *Nat. Nanotechnol.* **2015**, *10*, 517−521.
(6) Luo, Z.; Maassen, J.; Deng, Y.; Du, Y.; Garrelts, R. P.; Lundstrom, M. S.; Ye, P. D.; Xu, X. Anisotropic In-Plane Thermal Conductivity Observed in Few-Layer Black Phosphorus. *Nat. Commun.* **2015**, *6*, 8572.
(7) Yuan, H.-T.; Liu, X.-G.; Afshinmanesh, F.; Li, W.; Xu, G.; Sun, J.; Lian, B.; Curto, A. G.; Ye, G.-J.; Hikita, Y.; et al. Polarization-Sensitive Broadband Photodetector Using a Black Phosphorus Vertical p−n Junction. *Nat. Nanotechnol.* **2015**, *10*, 707−713.
(8) Zhao, S.; Wu, J.; Jin, K.; Ding, H.; Li, T.; Wu, C.; Pan, N.; Wang, X. Highly Polarized and Fast Photoresponse of Black Phosphorus-InSe Vertical p−n Heterojunctions. *Adv. Funct. Mater.* **2018**, *28*, 1802011.
(9) Wang, H.-W.; Chen, M.-L.; Zhu, M.-J.; Wang, Y.-N.; Dong, B.-J.; Sun, X.-D.; Zhang, X.-R.; Cao, S.-M.; Li, X.-X.; Huang, J.-Q.; et al. Gate Tunable Giant Anisotropic Resistance in Ultra-Thin GaTe. *Nat. Commun.* **2019**, *10*, 2302.
(10) Zhao, S.; Dong, B.; Wang, H.; Wang, H.; Zhang, Y.; Han, Z. V.; Zhang, H. In-Plane Anisotropic Electronics Based on Low-Symmetry 2D Materials: Progress and Prospects. *Nanoscale Adv.* **2020**, *2*, 109−139.
(11) Zhang, X.; Tan, Q.-H.; Wu, J.-B.; Shi, W.; Tan, P.-H. Review on the Raman Spectroscopy of Different Types of Layered Materials. *Nanoscale* **2016**, *8*, 6435−6450.
(12) Duesberg, G. S.; Loa, I.; Burghard, M.; Syassen, K.; Roth, S. Polarized Raman Spectroscopy on Isolated Single-Wall Carbon Nanotubes. *Phys. Rev. Lett.* **2000**, *85*, 5436−5439.
(13) Rao, A. M.; Jorio, A.; Pimenta, M. A.; Dantas, M. S. S.; Saito, R.; Dresselhaus, G.; Dresselhaus, M. S. Polarized Raman Study of Aligned Multiwalled Carbon Nanotubes. *Phys. Rev. Lett.* **2000**, *84*, 1820−1823.
(14) Kim, J.; Lee, J.-U.; Lee, J.; Park, H. J.; Lee, Z.; Lee, C.; Cheong, H. Anomalous Polarization Dependence of Raman Scattering and Crystallographic Orientation of Black Phosphorus. *Nanoscale* **2015**, *7*, 18708−18715.
(15) Zou, B.; Wei, Y.; Zhou, Y.; Ke, D.; Zhang, X.; Zhang, M.; Yip, C.-T.; Chen, X.; Li, W.; Sun, H. Unambiguous Determination of Crystal Orientation in Black Phosphorus by Angle-Resolved Polarized Raman Spectroscopy. *Nanoscale Horiz.* **2021**, *6*, 809−818.
(16) Lin, M.-L.; Leng, Y.-C.; Cong, X.; Meng, D.; Wang, J.; Li, X.-L.; Yu, B.; Liu, X.-L.; Yu, X.-F.; Tan, P.-H. Understanding Angle-Resolved Polarized Raman Scattering from Black Phosphorus at Normal and Oblique Laser Incidences. *Sci. Bull.* **2020**, *65*, 1894−1900.
(17) Ribeiro, H. B.; Pimenta, M. A.; de Matos, C. J. S.; Moreira, R. L.; Rodin, A. S.; Zapata, J. D.; de Souza, E. A. T.; Castro Neto, A. H. Unusual Angular Dependence of the Raman Response in Black Phosphorus. *ACS Nano* **2015**, *9*, 4270−4276.
(18) Ling, X.; Huang, S.-X.; Hasdeo, E. H.; Liang, L.-B.; Parkin, W. M.; Tatsumi, Y.; Nugraha, A. R. T.; Puretzky, A. A.; Das, P. M.; Sumpter, B. G.; et al. Anisotropic Electron-Photon and Electron-Phonon Interactions in Black Phosphorus. *Nano Lett.* **2016**, *16*, 2260−2267.
(19) Yan, Y.; Chen, L.; Dai, K.; Li, Y.; Wang, L.; Jiang, K.; Cui, A.; Zhang, J.; Hu, Z. Anisotropic Phonon Behavior and Phase Transition in Monolayer ReSe2 Discovered by High Pressure Raman Scattering. *J. Phys. Chem. Lett.* **2023**, *14*, 7618−7625.
(20) Kim, K.; Lim, S. Y.; Kim, J.; Lee, J.-U.; Lee, S.; Kim, P.; Park, K.; Son, S.; Park, C.-H.; et al. Antiferromagnetic Ordering in van Der Waals 2D Magnetic Material MnPS3 Probed by Raman Spectroscopy. *2D Mater.* **2019**, *6*, 041001.
(21) Choi, Y.; Kim, K.; Lim, S. Y.; Kim, J.; Park, J. M.; Kim, J. H.; Lee, Z.; Cheong, H. Complete Determination of the Crystallographic Orientation of ReX2 (X = S, Se) by Polarized Raman Spectroscopy. *Nanoscale Horiz.* **2020**, *5*, 308−315.
(22) Liu, Y.; Zou, J.; Chen, S.; Zhong, B.; Wang, Y.; Wang, H.; Huang, X. Raman Spectroscopy Studies of Black Phosphorus. *Spectrochim Acta A Mol. Biomol. Spectrosc.* **2022**, *271*, 120861.
(23) Song, Q.; Occhialini, C. A.; Ergeçen, E.; Ilyas, B.; Amoroso, D.; Barone, P.; Kapeghian, J.; Watanabe, K.; Taniguchi, T.; Botana, A. S.; et al. Evidence for a Single-Layer van Der Waals Multiferroic. *Nature* **2022**, *602*, 601−605.
(24) Koester, C. J. Achromatic Combinations of Half-Wave Plates. *J. Opt. Soc. Am., JOSA* **1959**, *49*, 405−409.
(25) Beckers, J. M. Achromatic Linear Retarders. *Appl. Opt., AO* **1971**, *10*, 973−975.
(26) Liu, J.; Cai, Y.; Chen, H.; Zeng, X.; Zou, D.; Xu, S. Design for the Optical Retardation in Broadband Zero-Order Half-Wave Plates. *Opt. Express, OE* **2011**, *19*, 8557−8564.
(27) Liu, X.-L.; Zhang, X.; Lin, M.-L.; Tan, P.-H. Different Angle-Resolved Polarization Configurations of Raman Spectroscopy: A Case on the Basal and Edge Plane of Two-Dimensional Materials. *Chinese Phys. B* **2017**, *26*, 067802.
(28) Castellanos-Gomez, A.; Buscema, M.; Molenaar, R.; Singh, V.; Janssen, L.; van der Zant, H. S. J.; Steele, G. A. Deterministic Transfer of Two-Dimensional Materials by All-Dry Viscoelastic Stamping. *2D Mater.* **2014**, *1*, 011002.
(29) Loudon, R. The Raman Effect in Crystals. *Adv. Phys.* **1964**, *13*, 423−482.
(30) Kaneta, C.; Katayama-Yoshida, H.; Morita, A. Lattice Dynamics of Black Phosphorus. *Solid State Commun.* **1982**, *44*, 613−617.
(31) Liu, T.; Xie, J.-L.; Leng, Y.-C.; Mei, R.; Wu, H.; Wang, J.; Li, Y.; Yu, X.-F.; Lin, M.-L.; Tan, P.-H. Quantitatively predicting angle-resolved polarized Raman intensity of black phosphorus flakes. *arXiv:2403.16053* **2024**, na.
(32) Mao, N.; Wu, J.; Han, B.; Lin, J.; Tong, L.; Zhang, J. Birefringence-Directed Raman Selection Rules in 2D Black Phosphorus Crystals. *Small* **2016**, *12*, 2627−2633.
(33) Pimenta, M. A.; Resende, G. C.; Ribeiro, H. B.; Carvalho, B. R. Polarized Raman Spectroscopy in Low-Symmetry 2D Materials: Angle-Resolved Experiments and Complex Number Tensor Elements. *Phys. Chem. Chem. Phys.* **2021**, *23*, 27103−27123.
(34) Huang, S.; Tatsumi, Y.; Ling, X.; Guo, H.; Wang, Z.; Watson, G.; Puretzky, A. A.; Geohegan, D. B.; Kong, J.; Li, J.; et al. In-Plane Optical Anisotropy of Layered Gallium Telluride. *ACS Nano* **2016**, *10*, 8964−8972.
(35) Li, X.-L.; Qiao, X.-F.; Han, W.-P.; Lu, Y.; Tan, Q.-H.; Liu, X.-L.; Tan, P.-H. Layer number identification of intrinsic and defective multilayer graphenes by the Raman mode intensity from substrate. *Nanoscale* **2015**, *7*, 8135−8141.
(36) Zhang, H.; Ni, Z.; Stevens, C. E.; Bai, A.; Peiris, F.; Hendrickson, J. R.; Wu, L.; Jariwala, D. Cavity-enhanced linear dichroism in a van der Waals antiferromagnet. *Nat. Photonics* **2022**, *16*, 311−317.
(37) Jones, R. C. A New Calculus for the Treatment of Optical SystemsI. Description and Discussion of the Calculus. *J. Opt. Soc. Am.* **1941**, *31*, 488−493.

https://doi.org/10.1021/acs.jpcc.4c07013
J. Phys. Chem. C 2024, 128, 21001−21008

Asymmetrical Angle-resolved Polarized Raman Intensity Profiles Measured by Commercial Half-wave Plates with Inevitable Retardance Error

Tao Liu,[†,‡,¶] Jia-Liang Xie,[†,‡,¶] Rui Mei,[†,‡] Miao-Ling Lin,[*,†,‡] and Ping-Heng Tan[*,†,‡]

†*State Key Laboratory of Superlattices and Microstructures, Institute of Semiconductors, Chinese Academy of Sciences, Beijing 100083, China*

‡*Center of Materials Science and Optoelectronics Engineering & CAS Center of Excellence in Topological Quantum Computation, University of Chinese Academy of Sciences, Beijing, 100049, China*

¶*These authors contributed equally to this work.*

E-mail: linmiaoming@semi.ac.cn; phtan@semi.ac.cn

Jones matrices of a half-wave plate with $\Delta\alpha$ in generalized form

In Jones-space, the polarization state of light is represented by a 2×1 Jones vector, while a polarization element is depicted by a 2×2 Jones matrix.[1] For a polarized light transmitting through a waveplate, an additional retardance (δ) will be introduced between the polarized components along fast and slow axes of the waveplate. For a half-wave plate (HWP), $\delta =$

180°. When the fast axis is aligned with the Z axis and the slow axis with the X axis in the laboratory coordinate system, the Jones matrix is given by:[1]

$$\mathbf{J}_0(\delta) = \begin{pmatrix} e^{-i\delta} & 0 & 0 \\ 0 & 1 & 0 \\ 0 & 0 & 1 \end{pmatrix}. \tag{S1}$$

When the waveplate is rotated along the Y-axis by β, the rotated Jones matrix can be written as:[1]

$$\begin{aligned} \mathbf{J}(\beta,\delta) &= \mathbf{T}(\beta)\mathbf{J}_0(\delta)\mathbf{T}(-\beta) \\ &= \begin{pmatrix} \cos\beta & 0 & -\sin\beta \\ 0 & 1 & 0 \\ \sin\beta & 0 & \cos\beta \end{pmatrix} \begin{pmatrix} e^{-i\delta} & 0 & 0 \\ 0 & 1 & 0 \\ 0 & 0 & 1 \end{pmatrix} \begin{pmatrix} \cos\beta & 0 & \sin\beta \\ 0 & 1 & 0 \\ -\sin\beta & 0 & \cos\beta \end{pmatrix} \\ &= \begin{pmatrix} \cos^2\beta e^{-i\delta} + \sin^2\beta & 0 & (1-e^{-i\delta})\cos\beta\sin\beta \\ 0 & 1 & 0 \\ (1-e^{-i\delta})\cos\beta\sin\beta & 0 & \cos^2\beta + \sin^2\beta e^{-i\delta} \end{pmatrix}, \end{aligned} \tag{S2}$$

where $\mathbf{T}(\beta)$ represents the rotation matrix. Let us define the retardance error $\Delta\alpha = \delta - 180°$, and the Jones matrix of the HWP becomes a function of β and $\Delta\alpha$:

$$\mathbf{J}(\beta,\Delta\alpha) = \begin{pmatrix} -\cos^2\beta e^{-i\Delta\alpha} + \sin^2\beta & 0 & (1+e^{-i\Delta\alpha})\cos\beta\sin\beta \\ 0 & 1 & 0 \\ (1+e^{-i\Delta\alpha})\cos\beta\sin\beta & 0 & \cos^2\beta - \sin^2\beta e^{-i\Delta\alpha} \end{pmatrix}. \tag{S3}$$

Indeed, when $\Delta\alpha = 0°$, Eq.(S3) transforms into Eq.(3), where $\beta = \theta/2$. This laboratory coordinate system described above aligns with the customary coordinate system for the BP flakes (Figure 1(b)). The customary coordinate system for $MoTe_2$ is different, where the initial fast axis is aligned with the X axis and the slow axis is aligned with the Y axis, as

shown in Figure 6(e), the initial Jones matrix and associated rotation matrix (with waveplate rotated along the Z axis by β) become:

$$\mathbf{J}_0'(\delta) = \begin{pmatrix} 1 & 0 & 0 \\ 0 & e^{-i\delta} & 0 \\ 0 & 0 & 1 \end{pmatrix}, \quad \mathbf{T}'(\beta) = \begin{pmatrix} \cos\beta & -\sin\beta & 0 \\ \sin\beta & \cos\beta & 0 \\ 0 & 0 & 1 \end{pmatrix}. \tag{S4}$$

The corresponding form of the Jones matrix (Eq.(9)) in the customary coordinate system of $MoTe_2$ can be derived from Eq. (S2).

General formulism of ARPR intensity profile measured by a half-wave plate with $\Delta\alpha$ and its non-dispersion approximation

The Jones matrix for imperfect HWP differ for the incident (laser) and Raman-scattered light (Raman signal), due to the incident and Raman-scattered light exhibiting different wavelengths. For clarity, let $\Delta\alpha_{\mathrm{i}}$ and $\Delta\alpha_{\mathrm{s}}$ represent the retardance errors of the HWP at the wavelengths for incident and Raman-scattered light, and $\mathbf{J}(\theta, \Delta\alpha_{\mathrm{i}})$ and $\mathbf{J}(\theta, \Delta\alpha_{\mathrm{s}})$ for the corresponding Jones matrices, respectively. By substituting $\mathbf{J}(\theta, \Delta\alpha_{\mathrm{i}})$ and $\mathbf{J}(\theta, \Delta\alpha_{\mathrm{s}})$ into Eq.(4), the Raman intensity of the A_g mode as a function of θ, $\Delta\alpha_{\mathrm{i}}$ and $\Delta\alpha_{\mathrm{s}}$ is derived

(similar to the Eq. (6) in main text):

$$
\begin{aligned}
I_{A_g}(\theta, \Delta\alpha_{\rm i}, \Delta\alpha_{\rm s}) &\propto \left| \boldsymbol{e}_{\rm s}^T \cdot J(\theta, \Delta\alpha_{\rm s})^{-1} \cdot \mathbf{R} \cdot J(\theta, \Delta\alpha_{\rm i}) \cdot \boldsymbol{e}_{\rm i} \right|^2 \\
&= |a|^2 \cos^2 \tfrac{\Delta\alpha_{\rm i}}{2} \cos^2 \tfrac{\Delta\alpha_{\rm s}}{2} \sin^4 \theta \\
&+ \tfrac{1}{16}|c|^2[4 - (1 - \cos 2\theta)(1 + \cos \Delta\alpha_{\rm i})][4 - (1 - \cos 2\theta)(1 + \cos \Delta\alpha_{\rm s})] \\
&+ 2|a||c| \cos\tfrac{\Delta\alpha_{\rm i}}{2} \cos\tfrac{\Delta\alpha_{\rm s}}{2} \sin^2\theta \left(\cos\tfrac{\Delta\alpha_{\rm i}}{2} \cos\tfrac{\Delta\alpha_{\rm s}}{2} \cos^2\theta - \sin\tfrac{\Delta\alpha_{\rm i}}{2} \sin\tfrac{\Delta\alpha_{\rm s}}{2} \right) \cos\Phi_{ac} \\
&- 2|a||c| \cos\tfrac{\Delta\alpha_{\rm i}}{2} \cos\tfrac{\Delta\alpha_{\rm s}}{2} \sin^2\theta \cos\theta \sin\tfrac{\Delta\alpha_{\rm i} + \Delta\alpha_{\rm s}}{2} \sin\Phi_{ac}.
\end{aligned}
\tag{S5}
$$

Here we only consider the case where both the wavelengths of the incident and the Raman-scattered light lie within the designed wavelength range of the HWP. For the cases that the wavelengths being outside the designed wavelength range of the HWPs, it becomes necessary to consider the most general form Eq. (S5). When the retardance errors of the HWP, $|\Delta\alpha_{\rm i}|$ and $|\Delta\alpha_{\rm s}|$, are small, the sum of first three terms is close to the intensity $I_{A_g}(\theta)$ measured with a ZHWP described by Eq.(4). Thus, the expression Eq.(S5) yields:

$$
I_{A_g}(\theta, \Delta\alpha_{\rm i}, \Delta\alpha_{\rm s}) \propto I_{A_g}(\theta) + \Delta I(\theta, \Delta\alpha_{\rm i}, \Delta\alpha_{\rm s}),
\tag{S6}
$$

where $\Delta I(\theta, \Delta\alpha_{\rm i}, \Delta\alpha_{\rm s}) \approx -2|a||c| \sin^2\theta \cos\theta \sin\frac{\Delta\alpha_{\rm i} + \Delta\alpha_{\rm s}}{2} \sin\Phi_{ac}$. In this case, the deviation on the ARPR intensity caused by retardance errors of the HWP is proportional to $\sin\left(\frac{\Delta\alpha_{\rm i} + \Delta\alpha_{\rm s}}{2}\right)$. If the wavelength difference between the incident and Raman-scattered light is negligible, a non-dispersion approximation for the retardance of HWPs gives $\Delta\alpha_{\rm i} \approx \Delta\alpha_{\rm s}$. Then the deviation on ARPR intensity from the results in ZHWP, $I_{A_g}(\theta)$, is proportional to $\sin(\Delta\alpha_{\rm i})$. Therefore, the estimated calculation error based on Eq.(S5) and further non-dispersion approximation (Eq. (7)) can be expressed as:

$$
\left| \sin\left(\tfrac{\Delta\alpha_{\rm i} + \Delta\alpha_{\rm s}}{2}\right) - \sin(\Delta\alpha_{\rm i}) \right| \approx 2 \sin\left(\tfrac{|\Delta\alpha_{\rm i} - \Delta\alpha_{\rm s}|}{2} \right).
\tag{S7}
$$

When $|\Delta\alpha_{\mathrm{i}} - \Delta\alpha_{\mathrm{s}}|$ is significant, it becomes necessary to take $\Delta\alpha_{\mathrm{i}}$ and $\Delta\alpha_{\mathrm{s}}$ into account separately. This is particularly important when the signs of $\Delta\alpha_{\mathrm{i}}$ and $\Delta\alpha_{\mathrm{s}}$ are opposite, as the value of $\Delta I(\theta, \Delta\alpha_{\mathrm{i}}, \Delta\alpha_{\mathrm{s}})$ could over twice that of $\Delta I(\theta, \Delta\alpha)$. In such cases, fitting with Eq. (S5) will yield more accurate results.

To roughly estimate the conditions of non-dispersion approximation for validity, it should be notice that in Fig. 2(c), ZHWPs show much poor wavelength compatibility when compared to AHWP#1. At λ_{ex} of 780 nm, the theoretical $|\Delta\alpha_{\mathrm{i}} - \Delta\alpha_{\mathrm{s}}|$ of the corresponding ZHWP reaches up to about 7.5° for the A_g^2 mode ($\sim$ 30 nm) of BP flakes. However, all the cases of ZHWPs shown in Fig. 3(a1, b1), Fig. 4(a) and Fig. 5 demonstrate that the ARPR intensity profiles measured by ZHWPs do not exhibit any appreciable asymmetry and match the fitted curves well based on Eq. (4). Consequently, at least for the cases satisfing $|\Delta\alpha_{\mathrm{i}} - \Delta\alpha_{\mathrm{s}}| < 7.5°$, the difference between $\Delta\alpha_{\mathrm{i}}$ and $\Delta\alpha_{\mathrm{s}}$ can be neglected feasibly. While for the cases of $|\Delta\alpha_{\mathrm{i}} - \Delta\alpha_{\mathrm{s}}| \geq 7.5°$, we would recommend considering Eq.(S5) for fitting the ARPR intensity profiles. A more precise criterion for $|\Delta\alpha_{\mathrm{i}} - \Delta\alpha_{\mathrm{s}}|$ may require additional experiments, yet this goes beyond the scope of this work.

In summary, if the retardance performance of a HWP is available, the necessity to account for $|\Delta\alpha_{\mathrm{i}} - \Delta\alpha_{\mathrm{s}}|$. Specifically, Eq. (4) is feasible for ZHWP cases (λ_{ex} being the specific designed wavelength), and Eq. (7) is applicable to the AHWP cases when $|\Delta\alpha_{\mathrm{i}} - \Delta\alpha_{\mathrm{s}}| < 7.5°$, otherwise one should consider Eq.(S5) with the cases of $|\Delta\alpha_{\mathrm{i}} - \Delta\alpha_{\mathrm{s}}| \geq 7.5°$. However, when the retardance curve of a HWP is unknown, Eq.(S5) should be recommended in fitting, taking into account the various factors discussed above.

Insensitive ARPR intensity of A_g^1 mode to $\Delta\alpha$

The Eq.(7) for Raman intensity of A_g mode as a function of θ and $\Delta\alpha$ can be divided into four terms:

$$\begin{aligned} I_{A_g}(\theta,\Delta\alpha) &\propto |\boldsymbol{e}_{\mathrm{s}}^T\cdot\mathbf{J}(\theta,\Delta\alpha)^{-1}\cdot\mathbf{R}\cdot\mathbf{J}(\theta,\Delta\alpha)\cdot\boldsymbol{e}_{\mathrm{i}}|^2 \\ &= |a|^2\cos^4\tfrac{\Delta\alpha}{2}\sin^4\theta + |c|^2\left(1-\sin^2\theta\cos^2\tfrac{\Delta\alpha}{2}\right)^2 \\ &+ 2|a||c|\cos^2\tfrac{\Delta\alpha}{2}\sin^2\theta\left(\cos^2\tfrac{\Delta\alpha}{2}\cos^2\theta-\sin^2\tfrac{\Delta\alpha}{2}\right)\cos\Phi_{ac} \\ &- 2|a||c|\cos^2\tfrac{\Delta\alpha}{2}\sin^2\theta\cos\theta\sin\Delta\alpha\sin\Phi_{ac}. \end{aligned} \tag{S8}$$

When $|\Delta\alpha|$ is small, the sum of first three terms is close to the intensity $I_{A_g}(\theta)$ measured with a ZHWP described by Eq.(4). Therefore, the Eq.(S5) can be approximated as:

$$\begin{aligned} I_{A_g}(\theta,\Delta\alpha) &\propto |\boldsymbol{e}_{\mathrm{s}}^T\cdot\mathbf{J}(\theta,\Delta\alpha)^{-1}\cdot\mathbf{R}\cdot\mathbf{J}(\theta,\Delta\alpha)\cdot\boldsymbol{e}_{\mathrm{i}}|^2 \\ &\approx I_{A_g}(\theta)+\Delta I, \end{aligned} \tag{S9}$$

where $\Delta I = -2|a||c|\cos^2\frac{\Delta\alpha}{2}\sin^2\theta\cos\theta\sin\Delta\alpha\sin\Phi_{ac}$. Due to the small Φ_{ac} for A_g^1 mode in BP flakes,[2–5] ΔI for A_g^1 mode should be close to zero. Thus, the ARPR intensity profiles of A_g^1 mode in BP flakes are insensitive to $\Delta\alpha$ when $\Delta\alpha$ is not large.

References

(1) Jones, R. C. A New Calculus for the Treatment of Optical SystemsI. Description and Discussion of the Calculus. *J. Opt. Soc. Am.* **1941**, *31*, 488–493.

(2) Kim, J.; Lee, J.-U.; Lee, J.; Park, H. J.; Lee, Z.; Lee, C.; Cheong, H. Anomalous Polarization Dependence of Raman Scattering and Crystallographic Orientation of Black Phosphorus. *Nanoscale* **2015**, *7*, 18708–18715.

(3) Ribeiro, H. B.; Pimenta, M. A.; de Matos, C. J. S.; Moreira, R. L.; Rodin, A. S.;

Zapata, J. D.; de Souza, E. A. T.; Castro Neto, A. H. Unusual Angular Dependence of the Raman Response in Black Phosphorus. *ACS Nano* **2015**, *9*, 4270–4276.

(4) Ling, X.; Huang, S.-X.; Hasdeo, E. H.; Liang, L.-B.; Parkin, W. M.;Tatsumi, Y.; Nugraha, A. R. T.; Puretzky, A. A.;Das, P. M.; Sumpter, B. G. et al. Anisotropic Electron-Photon and Electron-Phonon Interactions in Black Phosphorus. *Nano Lett.* **2016**, *16*, 2260–2267.

(5) Liu, T.; Xie, J.-L.; Leng, Y.-C.; Mei, R.; Wu, H.; Wang, J.; Li, Y.; Yu, X.-F.; Lin, M.-L.; Tan, P.-H. Quantitatively predicting angle-resolved polarized Raman intensity of black phosphorus flakes. *arXiv preprint* **2024**, *arXiv:2403.16053*, xxx.

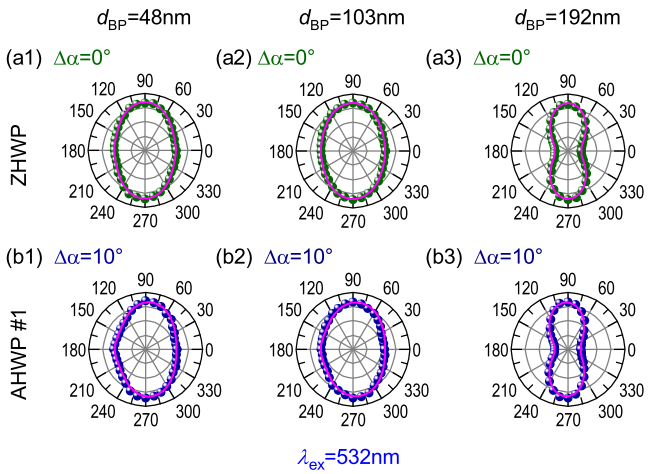

Figure S1: ARPR intensity profiles of A_g^1 mode in BP flakes with various d_{BP}, obtained with ZHWPs and AHWP#1 at λ_{ex} of 532 nm (a1-a3) show profiles obtained with ZHWPs, while (b1-b3) show profiles obtained with AHWP#1. The associated $\Delta\alpha$ values are annotated above each profiles.

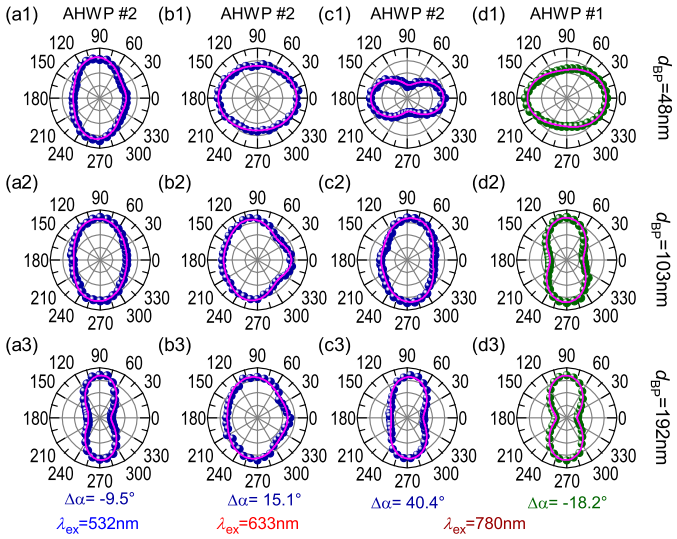

Figure S2: (a)-(c) ARPR intensity profiles of A_g^1 mode of BP flakes with different d_{BP}, measured with AHWP#2, with excitation wavelengths of 532 nm, 633 nm, and 780 nm, respectively. (d) ARPR intensity profiles of A_g^2 mode obtained with AHWP#1 under 780 nm excitation. The pink curves are the theoretical results using the mean $\Delta\alpha$ from A_g^2 mode in Table 1.